Journal of Energy Storage 165 (2026) 122359

Contents lists available at ScienceDirect

Journal of Energy Storage

journal homepage: www.elsevier.com/locate/est

Research Papers

Performance modeling of sodium-sulfur (NaS) batteries following optimized charging and discharging patterns

Botond Ilyés [a], Dávid Csemány [a,b,*], Martin János Mayer [a,b]

[a] Department of Energy Engineering, Faculty of Mechanical Engineering, Budapest University of Technology and Economics, Műegyetem rkp. 3, H-1111, Budapest, Hungary

[b] MTA-BME Lendület "Momentum" Renewable Energy Systems Research Group, Műegyetem rkp. 3, H-1111, Budapest, Hungary

ARTICLE INFO

Keywords:
Sodium-sulfur battery
Linear optimization
Battery energy storage system
Thermal modeling
Renewable energy integration

ABSTRACT

The integration of renewable energy sources into the power grid necessitates efficient and reliable energy storage solutions. Sodium-sulfur (NaS) batteries, with their high energy density and long cycle life, offer a promising option for large-scale storage applications. This study presents a comprehensive performance modeling framework for NaS batteries, combining linear programming-based optimization with a reduced-order thermal-electrochemical model to evaluate system behavior under realistic operating conditions. Two case studies are analyzed: a hybrid photovoltaic (PV) and battery system designed to meet 50% of a 10 GWh annual electricity demand at the lowest cost, and a stand-alone battery system to achieve the highest revenues for electricity market arbitrage. The results highlight the effectiveness of the proposed two-step modeling approach in optimizing system size and operation while ensuring thermal safety. The hybrid system requires 5.43 MW of PV capacity and 10.11 MWh of battery storage, achieving a round-trip efficiency of 87.84%. The stand-alone system, with the same system size demonstrated lower operational frequency and energy throughput, with slightly lower efficiency (85.26%) and similar cooling demand. Thermal analysis revealed that the optimized charging/discharging profiles necessitate enhanced cooling capacity beyond manufacturer specifications to maintain safe operating temperatures. The study underscores the limitations of linear optimization in capturing thermal constraints and suggests that future work should focus on integrated optimization frameworks that incorporate thermal dynamics. Additionally, refining the thermal management logic could further improve system efficiency and reliability. These findings contribute to the development of more robust and economically viable NaS battery systems for renewable energy integration.

1. Introduction

The transition to renewable energy sources such as solar, wind, and hydropower is critical for mitigating the environmental impact of fossil fuels and ensuring a sustainable energy future [1]. However, the inherent intermittency and variability of weather-dependent renewable energy generation pose significant challenges to grid stability and the reliable power supply [2]. To address these challenges, battery energy storage systems (BESS) are essential in enabling the seamless integration of variable renewable energy into the power grid by storing excess energy during periods of high generation and releasing it when generation is low [3]. Effective energy storage not only enhances grid stability but also contributes to reducing the reliance on conventional power plants and facilitates the transition toward a low-carbon energy system [4].

Among the various BESS technologies, sodium-sulfur (NaS) batteries have gained significant attention as a promising solution for large-scale energy storage, particularly in renewable energy applications [5]. NaS batteries utilize liquid sodium as the anode and sulfur as the cathode, operating at high temperatures (typically around 300 °C). This high-temperature operation allows sodium and sulfur to exist in liquid form, facilitating a highly efficient electrochemical reaction. NaS batteries are characterized by high energy density, long cycle life, and the use of abundant, low-cost raw materials, such as sodium, which provides a distinct advantage over other battery chemistries like lithium-ion batteries. Furthermore, the relatively low cost of sodium compared to lithium makes NaS batteries an attractive option for large-scale storage

* Corresponding author at: Department of Energy Engineering, Faculty of Mechanical Engineering, Budapest University of Technology and Economics, Műegyetem rkp. 3, H-1111, Budapest, Hungary.

E-mail address: csemany@energia.bme.hu (D. Csemány).

https://doi.org/10.1016/j.est.2026.122359
Received 21 January 2026; Received in revised form 27 March 2026; Accepted 21 April 2026
Available online 24 April 2026

applications, especially in regions where sodium resources are abundant [6]. In addition to their potential for cost-effective, large-scale energy storage, NaS batteries also exhibit several other key advantages, including high operating voltages and relatively high round-trip efficiency. These characteristics make NaS batteries particularly suitable for applications that require both high energy density and long-term reliability, such as grid stabilization, peak shaving, and renewable energy integration [7]. However, despite these promising features, the performance of NaS batteries is heavily influenced by their operating conditions, including the charging and discharging cycles. The battery's charge/discharge efficiency, cycle life, and overall performance can be significantly impacted by the charging rate, depth of discharge, and temperature fluctuations [8].

One of the key challenges in optimizing the use of BESS in renewable energy systems lies in developing strategies for efficient charging and discharging [9]. The performance of batteries can be sensitive to both the charging rate and the depth of discharge, with improper charging patterns leading to capacity degradation and reduced cycle life [10,11]. As a result, optimizing these charging and discharging patterns is crucial for improving the overall performance, longevity, and efficiency of batteries [12,13]. Furthermore, the integration of BESS with renewable energy sources necessitates that the storage system efficiently adapts to the intermittent and variable nature of renewable generation, which can fluctuate based on weather conditions and time of day [14]. Several studies have explored the potential of battery technologies for large-scale energy storage and grid applications. For instance, a study [15] demonstrated the feasibility of lead acid, lithium-ion (Li-ion), and nickel-metal hydride batteries for integrating renewable energy into the grid by effectively smoothing power fluctuations and ensuring stable voltage and frequency. Similarly, research by Attia et al. [16] highlighted the importance of optimizing charging and discharging protocols to minimize energy losses and extend the operational life of Li-ion batteries. However, despite the advances, there remains a gap in understanding the impact of different charging and discharging strategies on battery performance. This can be even more crucial for NaS batteries due to the lack of comprehensive analyses in literature, particularly under real-world operating conditions where renewable energy generation is highly variable.

Beyond system-level operational challenges, it is important to acknowledge that the performance of NaS batteries is also influenced by the intrinsic material properties of the electrodes. Improvements at the anode and cathode level, such as enhanced reaction kinetics, ionic transport, and structural stability, are often investigated using Density Functional Theory (DFT) and other atomistic simulation techniques [17]. These approaches provide valuable insights into electrode behavior at the microscopic scale and play a key role in guiding future material innovations. However, the present study focuses on commercially available NaS technology and investigates performance at the system level through an optimization-simulation framework. Since no new electrode materials are proposed or analyzed, incorporating DFT calculations would not directly support the objectives of this work, but we acknowledge their importance in the broader context of NaS battery development.

In addition to the optimization of operational parameters, the application of optimization techniques such as linear programming (LP) has shown significant potential in improving the design and operation of battery energy storage systems [18]. Linear programming, a mathematical method for determining the best possible outcome of a given model with linear objective function and constraints, can be used to optimize the charging and discharging schedules of BESSs, ensuring that energy is stored and released in the most efficient way possible [19]. By modeling the storage system as an LP problem, it is possible to minimize operational costs, reduce energy losses, and extend battery life, while satisfying the power demands and renewable energy generation variability [20]. In the context of battery technologies, LP can be employed to develop optimal dispatch strategies that balance the costs of storage, power generation, and maintenance, considering both economic factors and system constraints [21]. Several studies have successfully applied linear programming techniques to optimize BESS operation. For instance, the work by Amini et al. [22] demonstrated the application of LP for optimal charging and discharging of energy storage systems integrated with wind power, highlighting how it can improve the reliability and efficiency of the overall energy system. Similarly, Minh et al. [23] used LP to optimize energy storage management in microgrids with high renewable penetration, accounting for battery degradation, resulting in enhanced system performance. Consequently, the integration of LP in NaS battery modeling offers a systematic approach to improving performance and cost-efficiency in large-scale storage systems.

It is also important to emphasize that modeling NaS batteries differs fundamentally from modeling lithium-ion batteries. NaS cells operate at high temperatures, where both electrodes are in molten or semi-molten states, and the dominant heat generation mechanisms include not only Joule heating but also significant reversible (entropy-related) reaction heat. As a consequence, the thermal dynamics of NaS cells evolve on similar time scales as the electrochemical processes, making temperature an intrinsic state variable rather than a secondary correction as often assumed in Li-ion models. Furthermore, NaS batteries require continuous auxiliary heating to maintain operating temperature, which has no equivalent in Li-ion technology. Safety constraints are also fundamentally different: maintaining temperature within a narrow high-temperature band is essential to avoid solidification, internal structural stress, and polysulfide-related side reactions. In contrast, Li-ion batteries operate near ambient conditions, where thermal models typically focus on preventing overheating and degradation rather than on maintaining a minimum temperature. Due to these technology-specific characteristics, reduced-order NaS models rely heavily on temperature- and *SOC*-dependent resistance data, reaction entropy terms, and heating/cooling logic, all of which differ significantly from conventional Li-ion modeling approaches.

High operating temperatures pose significant technical challenges in NaS batteries [24], prompting numerous simulation studies on critical components. Min et al. [25] used finite volume methods to analyze solid electrolyte fractures and thermal runaway during abnormal cell operations, validating their model with experimental data. They found that increasing filler material density and reducing wick gap size can shorten the time to maximum temperature and slightly lower its peak, improving cell safety. Schaefer et al. [26] performed coupled thermal-electrical simulations to examine one-dimensional temperature distributions under various charge/discharge profiles. Their findings highlighted that higher operating temperatures improve efficiency but increase fire risks, necessitating robust thermal management systems and controlled current densities. Vudata and Bhattacharyya [27] investigated radial temperature distributions across cell configurations and cooling methods. They developed a reduced-order model for efficiency and recommended a hybrid cooling strategy using fans and phase-change materials to balance heat rejection variability, material costs, and fan power demands. Min and Lee [28] explored two modeling approaches: a detailed 3D finite volume model for spatial temperature distribution and a lumped parameter model for system-level simulations. Their multi-fidelity approach, validated with experimental data, emphasized heat dissipation analysis, thermal insulation optimization, and heater operation's impact on module efficiency.

The extensive thermal investigation of NaS batteries is extremely important. However, computationally feasible models are preferred in system-level analyses to keep the computational demand at a low level, especially in the case of long-term evaluations [29]. Comprehensive system-level optimization for NaS batteries is scarce in the literature. On one hand, the papers dealing with the detailed nonlinear modeling and performance assessment of NaS batteries generally rely on pre-defined sample charging profiles that do not reflect the optimal operation of the battery in practical applications. Such studies provide detailed insight into heat generation, failure mechanisms, and spatial temperature gradients [24–28], but they are not coupled with system-level dispatch optimization and therefore cannot evaluate the feasibility. On the other hand, optimization-driven studies for large-scale batteries (primarily involving Li-ion or generic BESS technologies [18–23,30–32]) tend to rely on simplified linear models and thus not being able to ensure the feasibility of the proposed operation is, e.g., from the perspective of thermal safety. As a result, the literature provides little guidance on how optimal long-term operation interacts with the characteristic thermal constraints of NaS batteries. The present study positions itself between these two research streams by combining linear programming with a NaS-specific thermal-electrochemical model, enabling a more integrated assessment than what is typically available in existing modeling and optimization studies. Therefore, the aim of this work is to fill this gap by presenting a two-step design process accounting for the nonlinearities and the thermal management of a NaS battery for optimized charging and discharging patterns, corresponding to two different case studies, enhanced through the application of linear programming. By providing a comprehensive understanding of NaS battery performance under various thermal conditions, the proposed model will contribute to the design of more efficient and reliable energy storage systems for renewable energy integration.

Consequently, the results of this study will provide valuable insights into the operational strategies needed to maximize the potential of NaS batteries in real-world energy systems. Unlike lithium-ion batteries, NaS batteries operate at high temperature, and their performance is strongly influenced by temperature-dependent resistance, reaction entropy heat, and auxiliary heating and cooling requirements. Capturing these effects within a computationally tractable framework requires a tailored modeling approach, which we establish through this two-step methodology. Moreover, the study provides year-long simulations for realistic operation, quantifying how optimized charging and discharging patterns interact with NaS-specific thermal constraints. Through this integrated analysis, we highlight both the benefits and the operational limitations of NaS technology, offering insights that are directly relevant for system-level planning and deployment.

The rest of the paper is structured as follows: Section 2 describes the utilized methods, including the linear optimization of the battery operation and the thermal-electrochemical model of the NaS battery. The two practical application cases are introduced in Section 3. The results are presented and discussed in Section 4, and Section 5 concludes the main findings.

2. Methods

The proposed model has two steps: 1) The sizing and operation of the battery and PV system are optimized using a simplified linear model based on historical time-series data of electricity prices, power consumption, and PV power output, and 2) the detailed operating conditions of the NaS battery are analyzed using a nonlinear thermal-electrochemical model of the technology. Cell current and voltage are calculated for the optimized state of charge (*SOC*) profile, allowing for a more accurate calculation of the efficiency considering its nonlinear dependence on the *SOC* and power. Battery cell temperature is also determined from the thermal balance of the battery, considering the internal heat dissipation and the external heating and cooling as well. Since the temperature is a crucial factor for NaS batteries, information about the thermal behavior of the optimized operation is essential.

2.1. Linear optimization problem

The sizing and operation of the hybrid PV and BESS system are optimized by linear programming. The model of the hybrid system must be considered with linear constraints. Unless noted differently, the equations introduced in this subsection apply to all N time steps. The electricity consumption and production must be equal in every time step, described as:

$$P_{load} + P_{ch} = P_{PV} + P_{dis} + P_{grid} \tag{1}$$

where P_{load} is the consumed power, P_{PV} is the power generated by the PV, P_{ch} and P_{dis} are the charging and discharging power of the battery, and P_{grid} is the power provided by the grid.

PV power can be used to charge the battery or to supply the demand. When surplus energy can be generated but there is no more available storage capacity or demand, PV power must be curtailed. The power output of the PV system can be described as:

$$P_{PV,inst} CF_{PV} = P_{PV} + P_{curt} \tag{2}$$

where $P_{PV,inst}$ is the nominal (installed) PV power, CF_{PV} is the time-dependent capacity factor of the PV system, and P_{curt} is the curtailed power.

Fully supplying the demand with a PV + BESS hybrid system is, although technically possible, not currently financially feasible in most cases. To model a more realistic scenario, part of the energy demand is allowed to be supplied by the grid. However, to ensure that at least a φ proportion of the consumption is covered by the PV system, the contribution of the grid is constrained as:

$$\sum_{t=1}^{N} P_{grid} \leq (1-\varphi) \sum_{t=1}^{N} P_{load} \tag{3}$$

The maximum charging and discharging power are limited by the rated power of the battery unit, which can be written as:

$$0 \leq P_{ch} \leq P_{mod} N_{mod} \tag{4}$$

$$0 \leq P_{dis} \leq P_{mod} N_{mod} \tag{5}$$

where N_{mod} and P_{mod} are the number and rated power of the battery modules.

The change of the energy stored in the battery between consecutive time steps is accounted for by the following constraint on the *SOC*:

$$SOC_{W,t} = SOC_{W,t-1} + \Delta t \left(\eta_b P_{ch,t-1} - \frac{P_{dis,t-1}}{\eta_b} \right) \Big/ C_{W,nom} \tag{6}$$

where subscripts W and t refer to the state of charge relative to the stored energy in Wh dimensions and the index of time step, respectively, Δt is the length of time step, η_b is the charging and discharging efficiency, and $C_{W,nom}$ is the total capacity of the battery pack in energy dimension, calculated as:

$$C_{W,nom} = C_{mod} N_{mod} \tag{7}$$

where C_{mod} is the capacity of a single battery module. $SOC_{W,t-1}$ is the *SOC* value at beginning of the previous time step, while $P_{ch,t-1}$ is the charging power in the previous time step.

Since SOC_W expresses the ratio of the stored energy compared to the usable energy storage capacity of the battery, it must always be between 0 and 1. Moreover, the initial *SOC*, denoted by subscript 0, is constrained to be the same as the *SOC* after the final time step, denoted by subscript N, to avoid the free energy that a higher initial than terminal *SOC* would introduce.

$$0 \leq SOC_W \leq 1 \tag{8}$$

$$SOC_{W,0} = SOC_{W,N} \tag{9}$$

The objective of the optimization is to achieve the highest economic value, which, however, depends on the application case. To that end, the objective functions of both case studies are introduced in Section 3.

The decision variables of the optimization are the installed capacities of the PV system and the NaS battery pack, reflecting the sizing of the system. Moreover, the values of the SOC_W, P_{ch}, P_{dis}, P_{grid}, P_{PV}, and P_{curt} at all N time steps are also decision variables, meaning that the power flow of the system and the operation of the battery are also determined by the optimization. The key result of the optimization is the SOC profile for the entire investigated time period, as it is the primary input to the thermal-electrochemical model.

The linear optimization method is widely used in design simulations of battery storage systems; however, since it relies on the entire yearly renewable power generation and market price data, it can only be performed in hindsight. During the operation of existing batteries, the optimization should rely on forecasts of these important parameters, which may result in slightly suboptimal performance. That said, the powerful AI models widely used in energy forecasting and related decision-making are expected to approximate optimal load profiles quite well in the long run.

2.2. Quadratic regularization term

Since the objective function only considers economic performance (see Section 3), it is possible that different charging and discharging profiles may result in the same economic outcome. Examples include cases where the overproduction of a PV system is either curtailed or charged into the battery, and the only goal is to fill the storage by the end of the day, regardless of the charging profile during the day. Similarly, longer periods with constant electricity prices can lead to the same situation in case of either charging or discharging.

Mathematically, this means that the optimization problem is underdetermined, and there are multiple optimal feasible solutions. The LP solver always returns a single basic feasible solution, which is a corner point of the feasible region that tends to push decision variables to their bounds, resulting in an oscillating charging profile between the zero and maximum values, as shown in Fig. 1A. However, high charging and discharging powers generally reduce the efficiency; therefore, uniform profiles would better reflect the real operation of the battery in such situations. One possible solution to make the solver return smooth, average charging profiles instead of extreme values is to include a quadratic penalty term in the objective function.

$$\Pi = \mu \sum \left(P_{ch}^2 + P_{dis}^2\right) \tag{10}$$

where μ is the parameter that adjusts the strength of the quadratic penalty term. High parameter values cause the optimization to reduce the charging and discharging power peaks even at the cost of deteriorating the economic performance. In contrast, low values, such as $\mu = 10^{-8}$ used in this study, indicate that the economic objective is prioritized, and the peak power is only reduced as long as it does not compromise the economic value.

The effect of the quadratic penalty term is visualized in Fig. 1. The linear optimization results in charging power fluctuating between zero and the maximum during both days, as well as fluctuations in discharging power in the morning of the first day and at the end of the second day. The quadratic penalty term smooths the charging and discharging power values during all these periods, resulting in a more balanced operation, while the objective functions remain unchanged for the first five digits.

It is important to note that thermal constraints cannot be directly incorporated into the linear or quadratic programming formulation used in this study. The cell temperature evolution depends on strongly nonlinear relationships, such as the temperature- and SOC-dependent internal resistance, the entropy term, and the discrete switching logic of the heating and cooling system, which would transform the optimization problem into a nonlinear or mixed-integer nonlinear program. Solving such a model over a full year of data with minute-scale thermal resolution would result in prohibitive computational complexity and would not be compatible with the system-level planning purpose of this work. For this reason, the optimization provides an economically optimal dispatch profile, and the detailed thermal-electrochemical model is subsequently applied a posteriori to evaluate the feasibility of the resulting operation. This two-step methodology preserves tractability while still enabling a rigorous assessment of thermal safety.

The quadratic penalty function transforms the LP into a quadratic optimization (QP) problem. However, since all constraints are still linear and the objective function is convex, the QP problem can still be solved easily in many solvers, only at the cost of a slightly longer runtime. In this study, the optimization problem is implemented and solved using Gurobi, which efficiently handles both the LP and QP formulations of the problem, despite its high dimensionality.

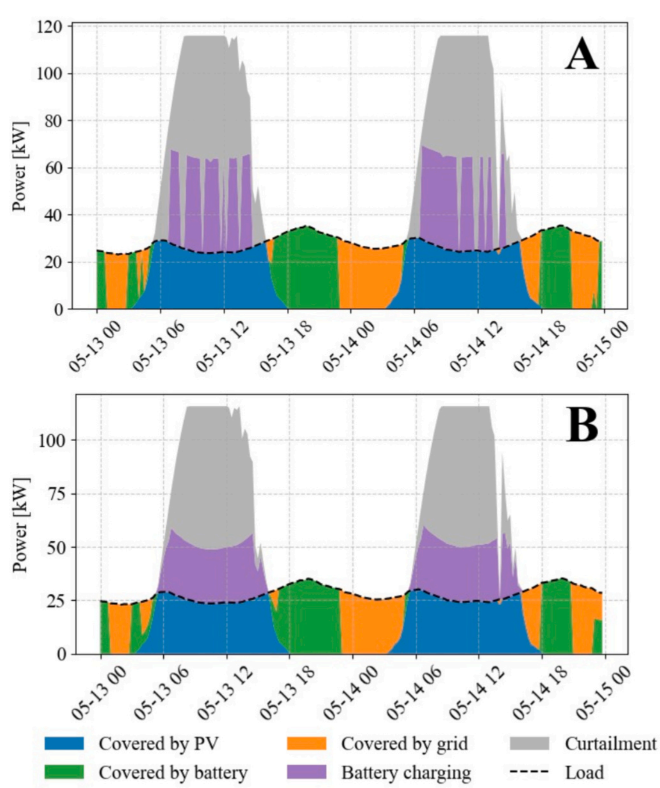

Fig. 1. Illustration of the optimized battery charging and discharging power without (top) and with (bottom) the quadratic penalty term.

2.3. Thermal-electrochemical battery model

The thermal behavior of the battery must be analyzed to ensure normal and safe operation. Consequently, a thermal-electrochemical model has been developed, which is the reduced version of the lumped parameter model of the NaS battery presented in [29], which was previously validated against experimental data. The most important simplifications and model reductions are neglecting the detailed modeling of the convective thermal loss to the environment and the detailed cooling system and considering these heat flow rate values as constants, provided by the manufacturer. These assumptions are reasonable if extremely high-temperature abnormal operation is not evaluated, which is valid for the current investigation. As a result of the simplification, numerical stability can be preserved despite the increased time step compared to the original model, facilitating the reduction of the computational demand [29].

The key equations of the thermal-electrochemical model are presented below, while readers are referred to [29] for a more detailed description of the model. The open-circuit voltage (V_{OC}) can be calculated by linear interpolation based on SOC_A according to [33]. Subscript A refers to the state of charge relative to the sored energy in Ah dimensions. The conversion between SOC_W and SOC_A is discussed in Section 2.4. The cell resistance, R_{cell}, depends on SOC_A, the cell temperature, and whether charging or discharging takes place [33]. In the presented model, R_{cell} is interpolated from the tabulated datasets with 0.05 SOC_A and 20 °C temperature resolution using the profiles from [33]. Since cell resistance data is available for state of charge range of 10–90% from [33], the analyses presented in this paper correspond to the same range. Cell current, which is positive for charging and negative for discharging, and voltage in the actual time step are calculated as follows:

$$I_{cell,\tau} = \frac{SOC_{A,\tau} - SOC_{A,\tau-1}}{\Delta\tau} \tag{11}$$

$$V_{cell} = V_{OC} + I_{cell}R_{cell} \tag{12}$$

where τ is the index of the time series data points in the battery simulation, and $\Delta\tau$ is the length of a time step. Please note that τ and $\Delta\tau$ are different from t and Δt; therefore, the are noted differently.

Based on the cell current and the number of modules and cells (N_{cells}), the instantaneous charging and discharging power can be calculated, as:

$$P = I_{cell}V_{cell}N_{mod}N_{cells} \tag{13}$$

During the operation, Joule-heat dissipation and reaction heat are generated. The corresponding heat flow rates are calculated as:

$$\dot{Q}_{Joule} = \frac{(V_{cell} - V_{OC})^2}{R_{cell}} \tag{14}$$

$$\dot{Q}_{reaction} = I_{cell}T_{cell}\frac{\mathrm{d}E}{\mathrm{d}T_{cell}} \tag{15}$$

while the thermal loss to the environment ($\dot{Q}_{loss}$) is approximated by −900 W. $\mathrm{d}E/\mathrm{d}T_{cell}$ is the entropy term, which is a negative value and depends on the SOC_A, detailed in [29]. Please note that the reaction heat rate is positive during discharging and negative during charging. The cooling and heating logic has been implemented based on the manufacturer's specifications as follows (see [29] for further details):

- If cell current is negative (discharging mode), cooling is operated at nominal power.
- If the cell current is positive (charging mode) in the previous time step and the cell temperature is higher than the cooling limit temperature and SOC is lower than the cooling limit SOC, the cooling is operated at nominal power.
- If the cell temperature in the previous time step is lower than the heating limit temperature, then heating is operated at nominal power.
- If cell temperature is higher than the heating limit temperature and lower than the turn-off limit and heating was operated, then heating is operated at nominal power.

The cooling and heating thermal power for a module, as specified by the manufacturer, are −1200 W and 4300 W, respectively. The electric power of the cooling fan is 67 W. Cell temperature is calculated from the thermal balance of one battery module as:

$$T_{cell,\tau} = \frac{N_{cells}\cdot\left(\dot{Q}_{joule,\tau} + \dot{Q}_{reaction,\tau}\right) + \dot{Q}_{loss,\tau} + \dot{Q}_{cooler,\tau} + \dot{Q}_{heater,\tau}}{N_{cells}\cdot c_{cell}\cdot\rho_{cell}\cdot\frac{d_{cell}^2\cdot\pi}{4}\cdot h}\cdot\Delta\tau + T_{cell,\tau-1} \tag{16}$$

where c_{cell} is the specific heat capacity, ρ_{cell} is the cell density, d_{cell} is the diameter, while h is the height of the cylindrical cell.

As indicated in Eq. (11), thermal calculations can only be performed if the state of charge level at the next time step is known in advance. Since optimization is based on historical data and the SOC profile is the result, this condition is fulfilled in our case because the SOC profile is known for the whole analyzed period. However, for the real-time application of the model, performance-based calculations will be more relevant, since battery operation can be planned based on the expected demand. In addition, temporal resolution is also an important aspect, since the smaller the time step, the more accurate the approximation. In [29], a time step of 1 s is used, which is significantly less than the 15-min resolution normally used in the power system. To that end, using this latter would introduce significant distortions in the thermal operation of the battery. Consequently, 1-min resolution is used during the thermal calculations by resampling the 15-min resolution SOC profiles obtained by the optimization to 1-min resolution using linear interpolation. This improves the accuracy of the calculations without a significant increase in the runtime, whereas interpolating to an even higher resolution did not bring significant changes in the results. This is justified in Appendix A.

During the optimization, the same constant efficiency value was considered for both charging and discharging, however with the addition of internal resistance calculations instantaneous efficiency values can also be calculated. The power used during these calculations considers the thermal behavior of the battery thereby providing a more accurate description of the operation.

$$\eta_{ch,\tau} = \frac{\left(SOC_{W,\tau} - SOC_{W,\tau-1}\right)C_{W,nom}}{P\Delta\tau} \tag{17}$$

$$\eta_{dis,\tau} = \frac{P\Delta\tau}{\left(SOC_{W,\tau} - SOC_{W,\tau-1}\right)C_{W,nom}} \tag{18}$$

2.4. Model coupling

As it was mentioned before, most of the battery models, including the lumped parameter NaS model at hand, define SOC in terms of the electric charge stored in the battery, i.e., in Ah dimension, denoted as SOC_A. In contrast, the SOC profiles obtained by the linear optimization are in terms of the stored energy, i.e., in Wh dimensions, denoted by SOC_W. Like in the case of other battery chemistries, the open-circuit voltage of the NaS battery is not constant but depends on the SOC_A as shown in Fig. 2, therefore, SOC_W and SOC_A are not equivalent and interchangeable [29].

To couple the linear optimization and the detailed thermal model, one should first establish a conversion relationship between SOC_W and SOC_A. The OCV–SOC_A function has a linear increasing part below 45%

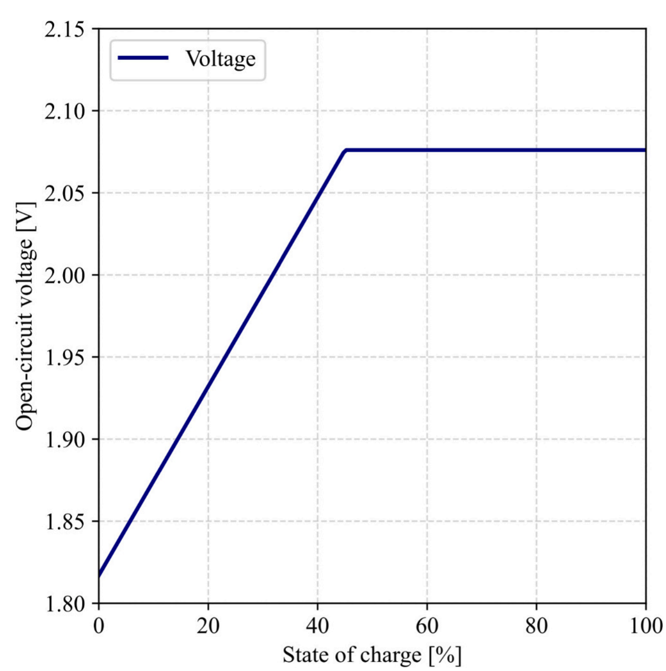

Fig. 2. Open-circuit voltage as a function of the Ah SOC.

SOC_A and constant part above that, which suggests that the $SOC_W - SOC_A$ relationship has a quadratic and a linear part.

The conversion relation is based on the open-circuit voltage function in terms of the SOC according to [33]:

$$SOC_{W,br} = \frac{(V_{max} + V_{min})C_{A,br}}{2C_{W,nom}} \tag{19}$$

where V_{min} and V_{max} are the minimum and maximum V_{OC}, $C_{A,br}$ is the total storage capacity in Ah dimension at 45% charge level, and $C_{W,nom}$, calculated by multiplying the module capacity and the number of modules (N_{mod}), is the nominal capacity of the battery in Wh. Based on the current battery parameters, the calculated values of $SOC_{W,br}$ is 43.1%.

Fig. 3 showcases the conversion of the SOC_W to SOC_A. If SOC_W is lower than $SOC_{W,br}$, then the conversion should be performed by Eq. (20), where $C_{A,nom}$ is the nominal capacity of the whole battery in Ah. Otherwise, the conversion is described by Eq. (21).

$$SOC_A = \frac{-V_{min}C_{A,nom} + \sqrt{\left(V_{min}C_{A,nom}\right)^2 - 4\frac{V_{max}-V_{min}}{C_{A,br}}\frac{C_{A,nom}^2}{2}SOC_w C_{W,nom}}}{2\frac{V_{max}-V_{min}}{C_{A,br}}\frac{C_{A,nom}^2}{2}} \tag{20}$$

$$SOC_A = \frac{SOC_w C_{W,nom} - SOC_{W,br} \cdot C_{W,nom} + V_{max} \cdot C_{A,br}}{V_{max} \cdot C_{A,nom}} \tag{21}$$

Although the present reduced-order model uses empirical *OCV-SOC* and resistance-*SOC* curves from [33] to describe the electrochemical behavior of the NaS cell, the characteristic shape of the *OCV* curve in Fig. 2 originates from the multistep sulfur reduction sequence in the cathode. During discharge, sulfur is gradually converted into sodium polysulfides in a multistep reaction sequence. Each step inserts two additional sodium atoms and transfers two electrons, progressively increasing the sodium content and modifying the molar mass of the active material. As a result, the partial specific capacities increase toward lower-order polysulfides, reaching the maximum at the fully reduced product Na_2S, since each polysulfide equilibrium contributes differently to the overall potential [5]. Because our thermal-electrochemical model relies on tabulated *OCV* and resistance curves

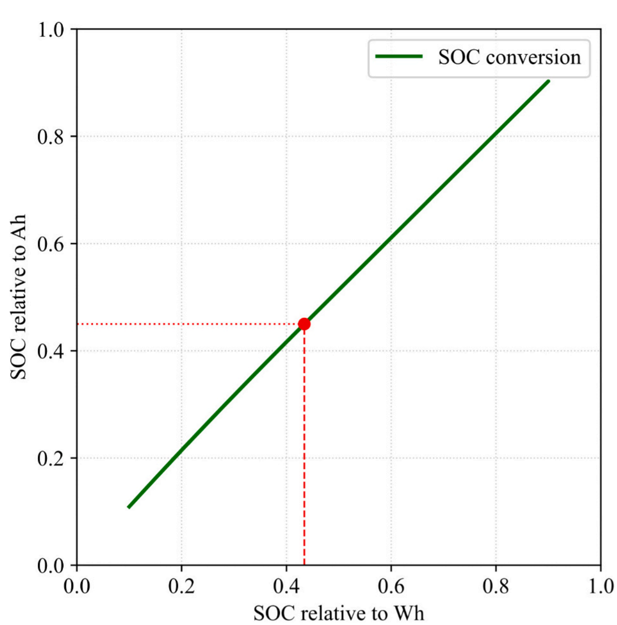

Fig. 3. State of charge in terms of Wh and Ah dimensions. Dashed red lines indicate $SOC_{A,br}$ and $SOC_{W,br}$. (For interpretation of the references to color in this figure legend, the reader is referred to the web version of this article.)

rather than explicit polysulfide kinetics, these reactions are not modeled individually. However, their capacity contributions provide the physical foundation of the *OCV-SOC* relationship used for the SOC_W-SOC_A conversion.

3. Practical application cases

In this section, two case studies are presented to assess two different installation conditions and operating strategies of the battery system. Input parameters of the analyses are the electricity prices on the day-ahead market (DAM), electric power generation of a theoretical PV power plant, and a load profile, shown in Fig. 4. For the PV generation data, 10-min weather observation data from the HungaroMet Budapest Pestszentlőrinc meteorological station is interpolated to 15 min, and then a physical PV model chain [34] is used to generate simulated power output data for a south-facing solar PV array with a 30° tilt angle and 80% inverter sizing factor (AC/DC nominal power ratio).

The load profile is based on the Hungarian electricity system load, obtained from the datadase[1] of the Hungarian Transmission System Operator, and normalized to a total annual consumption of 10 GWh. Electricity prices are from the data publication[2] of the organized Hungarian spot power exchange. All data are in 15-min resolution and cover the full calendar year of 2024.

Additional input data of the model are the technological and financial parameters of the PV and battery system. It is important to emphasize that a considerable variation can be observed in the literature regarding investment and maintenance costs. However, there is currently one manufacturer on the market from whom the technology can be purchased commercially. The input parameters are summarized in Table 1.

3.1. Case 1: hybrid PV-battery system

In the first scenario, the battery is connected to a PV system with the aim of shifting the power production to cover a higher share of the electric load. In this case, 1) the battery can only be charged by the PV, i.e., $P_{ch} \leq P_{PV}$, and 2) the battery can only be discharged to supply the load, but cannot feed power to the grid, i.e., $P_{grid} \geq 0$. The $\varphi = 50\%$ of the 10 GWh annual demand is set to be covered by the hybrid system. In this case, the battery cooperates with the PV system by storing the surplus energy and utilizing it to cover the load when the PV power is insufficient and the market prices are high.

The objective of the optimization is to ensure the lowest-cost energy supply considering the installation and operation and maintenance (O&M) costs of the hybrid system and the cost of the power purchased from the grid. The objective function, inspired by [36], is written as follows:

$$\min\left(c_{PV}P_{PV,inst}(\varepsilon_{PV} + l_{PV}) + c_b\left(\varepsilon_b N_{mod} C_{nom} + l_b \sum P_{ch}\right) + \sum P_{grid} c_{el} \Delta t + \Pi\right) \tag{22}$$

where c_{PV} and c_b are the specific installation costs, ε_{PV} and ε_b are the capital recovery factors, and l_{PV} and l_b are the O&M factors of the PV and battery, respectively, c_{el} is the DAM electricity price, and Π is the quadratic penalty term introduced in Section 2.2. Note that the O&M costs of the battery are considered to depend on the operational activity of the battery, hence the overall charging performance over the year, on the purpose to account for the costs associated with the battery degradation in the model. The capital recovery factors are described as:

$$\varepsilon_{PV} = \frac{1}{1 - \frac{1}{(1+r)^{T_{PV}}}} \tag{23}$$

[1] MAVIR Zrt, https://www.mavir.hu/web/mavir/rendszerterheles.
[2] HUPX Zrt., https://labs.hupx.hu/view/DAM_Aggregated_Trading_Data_v1.

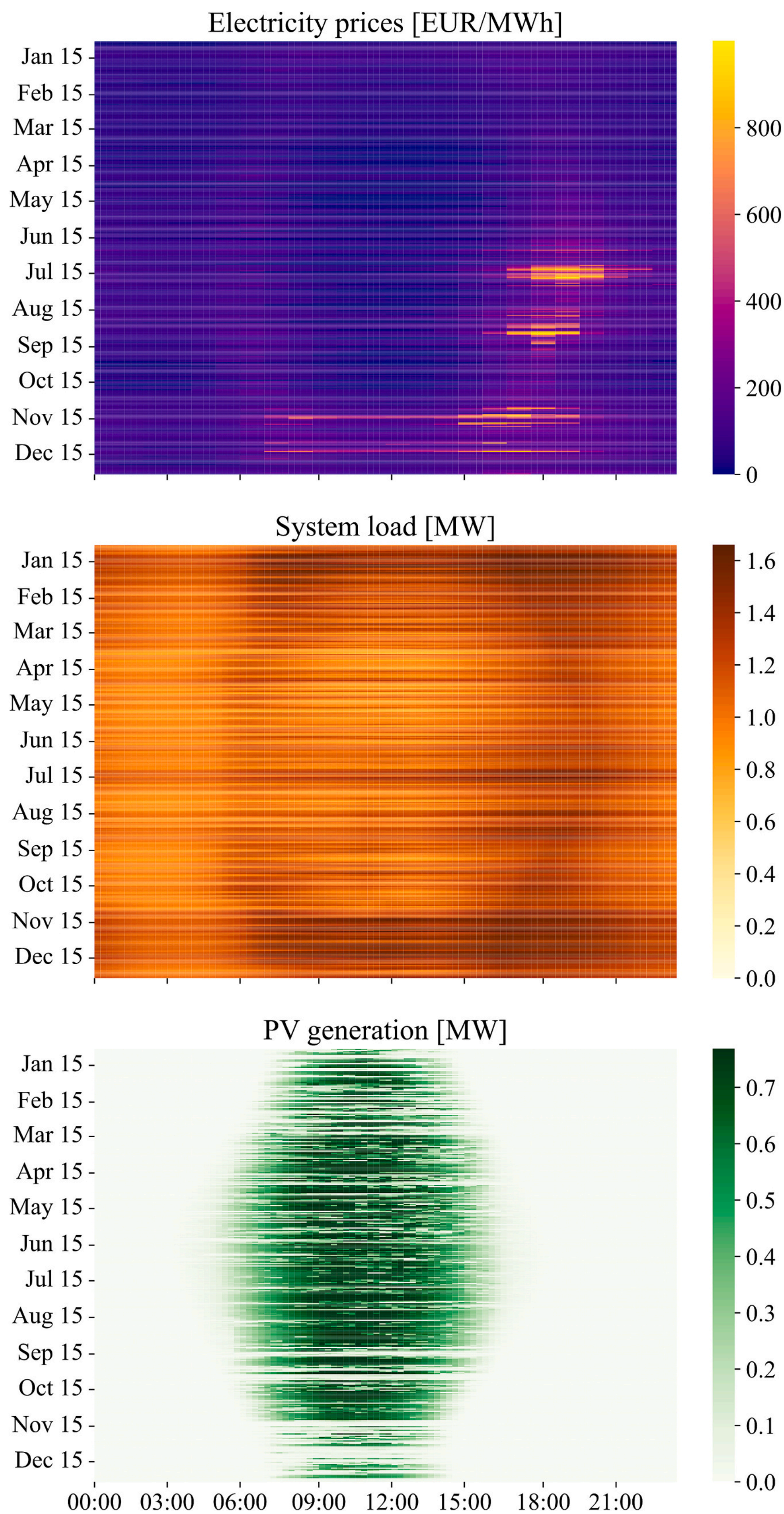

Fig. 4. System load and electricity prices.

Table 1
Technical and financial input parameters of the analyses [30–32,35].

	Parameter	Value
Optimization data	Renewable coverage ratio (φ)	50%
	PV specific cost (c_{PV})	600 EUR/kW
	Battery specific cost (c_b)	280 EUR/kWh
	PV O&M cost factor (l_{PV})	1% of the investment cost
	Battery O&M cost factor (l_b)	0.02% of the investment cost
	Battery charging/discharging efficiency (η_b)	90%
	Lifetime of the PV system (T_{PV})	30 years
	Lifetime of the battery (T_b)	15 years
	Optimization time step (t)	15 min
	Discount rate (r)	8%
Thermal analysis data	Maximum cell voltage (V_{max})	2.076 V
	Minimum cell voltage (V_{min})	1.817 V
	Cell capacity ($C_{A,nom}$)	725 Ah
	Number of cells in a battery module (N_{cells})	192
	Module capacity (C_{mod})	250 kWh
	Average specific heat capacity (c_{cell})	1103.8 J/(kg•K)
	Average cell density (ρ_{cell})	2247.1 kg/m^3
	Cell diameter (d_{cell})	0.09 m
	Thermal analysis time step (τ)	60 s
	Cooling power specified by the manufacturer ($\dot{Q}_{cooler}$)	−1200 W
	Input electric power of the cooling fan (P_{fan})	67 W
	Heating power specified by the manufacturer ($\dot{Q}_{heater}$)	4300 W
	Heat loss ($\dot{Q}_{loss}$)	−900 W

$$\varepsilon_b = \frac{\tau}{1 - \frac{1}{(1+r)^{T_b}}} \tag{24}$$

where r is the discount rate, and T_{PV} and T_b are the lifetimes of the PV system and the battery, respectively.

3.2. Case 2: electricity market arbitrage

In the second scenario, the battery is connected directly to the grid without a PV system and load, i.e., $P_{PV} = 0$ and $P_{load} = 0$. The goal of the battery is to obtain the highest possible revenue from arbitrage activity in the DAM. The objective function of this optimization is:

$$\max\left(\sum (P_{dis} - P_{ch}) c_{el} \Delta t - \Delta t c_b l_b \sum P_{ch} - \Pi \right) \tag{25}$$

At each time step, the battery can be charged, discharged or be in stand-by mode, but charging and discharging cannot occur simultaneously.

4. Results and discussion

The presentation of the results is organized around the different aspects of the evaluation, such as the battery operation, thermal management, and charging and discharging efficiency. In accordance, the results for Case 1 and Case 2 are discussed in parallel and compared to show how the application case affects the different aspects of the operation.

4.1. Optimal sizing and operation

In Case 1, the optimal installed capacities for supply 50% of the 10 GWh annual electricity consumption are 5.43 MW nominal PV power and 10.11 MWh NaS capacity, which latter corresponds to 36 battery modules and 1.68 MW nominal power, considering the 6-hour storage time. For comparison, the annual electricity consumption of Hungary is around 40 TWh, which is 4000 times higher than the value used in this case study. In addition to the system size, the optimization also determines the operation of the hybrid system considering the PV power, the electricity demand, and the market prices while determining the optimal charging and discharging cycles. The power flows are illustrated in Fig. 5 for a sample 5-days period.

Even despite the utilization of a battery, the curtailment of the PV is still significant due to the limited storage capacity. This is in-line with the concept that overbuilding and curtailment are key elements of cost-effectively achieving high renewable coverage with a PV–battery hybrid system [37]. In the daytime, when PV power is high, the battery is charging and grid power is zero. The fluctuations and rapid changes in the power flows are due to the temporal resolution of the optimization and the price-based optimization. The batteries usually discharge in the evening hours when electricity prices are high. Grid power is significant during transition periods and when PV power is lower, usually on days with cloudy weather, as can be seen on 17 May. Typically, one full cycle occurs on clear days with sufficient PV production to have enough surplus for battery charging, while the battery is not operated on overcast days with low PV power that does not exceed the load.

In Case 2, the same 10.11 MWh battery is used only for arbitrage activity, resulting in the power flow shown in Fig. 6. The battery operation is directly linked to the market prices, with the battery charging either at midday or night when electricity prices are low and discharging in the morning and evening hours when electricity prices are high. Due to the costs associated with degradation, the battery only charges and discharges when there is a sufficient difference between the respective market prices, resulting in a less frequent operation compared to Case 1.

To provide an overview of the battery operation for the whole year instead of only a sample period, the state of charge, temperature, charging and discharging power, and efficiency of the batteries are shown on heatmaps for the whole year in Figs. 7 and 8 for Case 1 and Case 2, respectively.

For now, the discussion is limited to A and C subplots of these figures, indicating the state of charge and power profiles, respectively. The charging and discharging power values apply for a single battery module, are positive when the battery is charging and negative when discharging, and do not consider the energy demand of the thermal management system, which is assumed to be covered by an external source.

Comparing the two cases, the state of charge profiles highlight the difference in battery activity mentioned earlier. In Case 1, battery charging aligns well with the PV production, as shown in Fig. 4. The timing of the discharge aligns well with the hours of highest market prices each day, however, the length of the discharge period each day depends on the charged energy and thus indirectly on the PV production of the given day. In Case 2, the battery is mostly charged during the night in most of the year, and daytime charging appears sometimes in the summer, even despite the significant installed PV capacity in the Hungarian system. The typical charging and discharging times are around 1 to 4 h, even though it takes 6 h for the storage to fully charge or discharge, which suggest that the operation of the battery is limited by the typical short durations of extremely low or high prices and the nominal power of the battery.

The main characteristics of the battery operation are summarized in Table 2. The number of equivalent cycles is 200 in Case 1, reflecting that the operation of the battery is limited when the PV production is insufficient. In Case 2, the number of equivalent charging cycles is only 141.5, which is 0.39 cycles per day on average, even though there are many days with two charging (night and midday) and two discharging (morning and evening) periods a day. That said, the number of cycles is limited by the low duration of the charging and discharging periods and the days when the market price spread (i.e., the difference between the highest and lower price during a day) is too low to cover the degradation of the battery. Under the boundary conditions of the present study, the hybrid operation leads to a better utilization of the battery with 41%

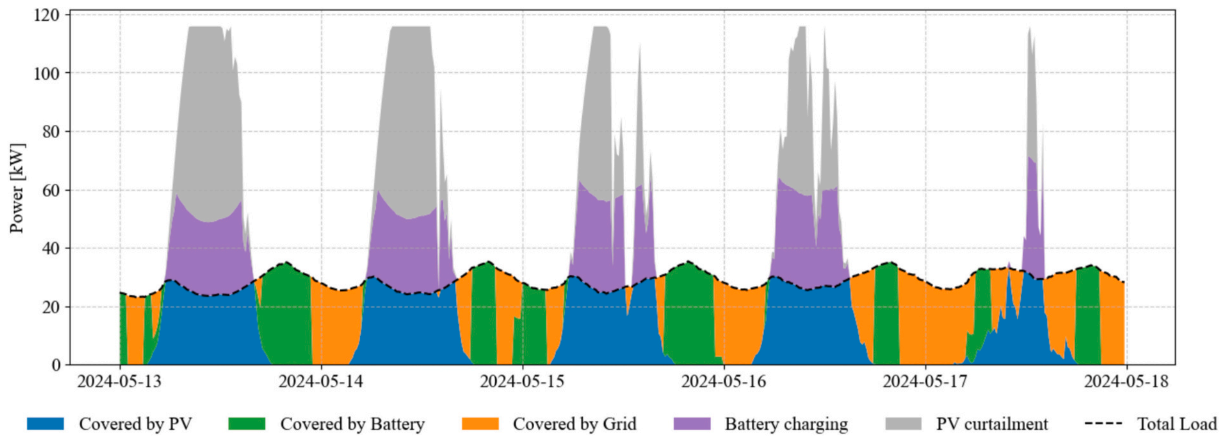

Fig. 5. Power flows of the hybrid system and the load for a sample period in Case 1.

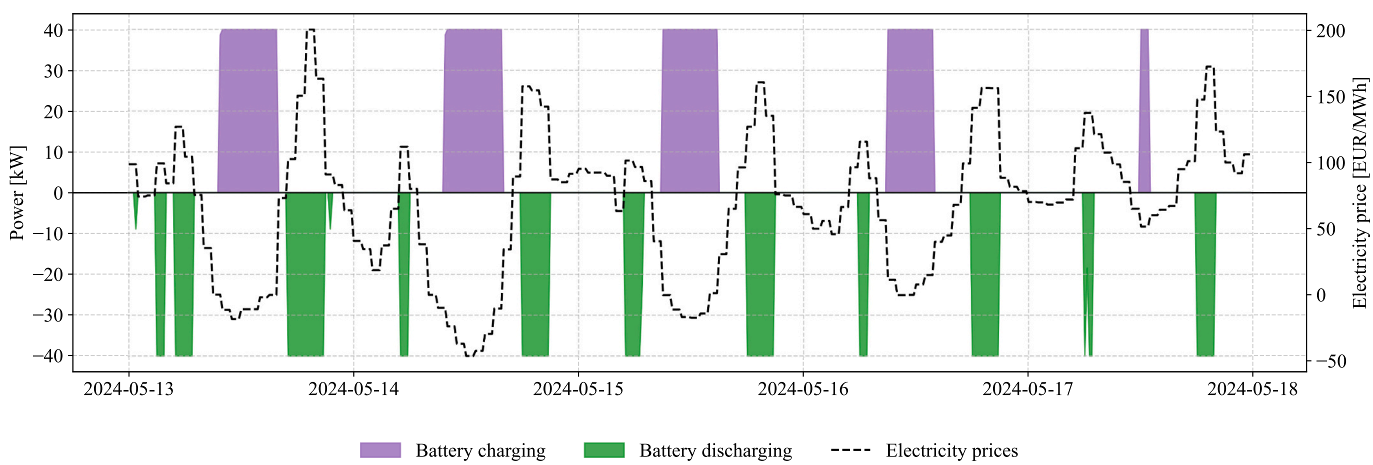

Fig. 6. Power flow of the battery and the electricity prices for a selected period for Case 2.

more cycles compared to the arbitrage operation. However, whereas the operation of the battery is constrained by the PV system, the operation for arbitrage depends on the market prices, therefore, the number of cycles can significantly increase if the prices become more volatile as it was for example in 2022.

The round-trip efficiency values shown in Table 2 do not consider the additional energy used for the thermal management of the battery. In most cases, this can be covered by the battery, lowering the amount of energy that can be discharged. However, since during the optimization, the thermal constraints cannot be considered, we suppose that this energy is supplied by an external source. This also leads to higher efficiency values and higher amount of energy that can fed back into the grid. The efficiency values are mostly influenced by the range the battery is operating in and the internal resistance values. The amount of energy used for thermal management is quite significant compared to the energy stored during the investigated period.

The number of yearly cycles is low compared to the cycle lifetime of the battery. A NaS cell requires 7300 cycles to suffer a capacity loss from the nominal value of 725 Ah to 525 Ah [35]. The 141–200 cycles result in around 5–6 Ah capacity loss, which is less than 1% of the nominal cell capacity, proving that neglecting capacity reduction for the present analyses is a reasonable assumption. To justify this, calculations were performed for 720 Ah cell capacity and the results were compared to the values indicated in Table 2, showing no noticeable differences.

4.2. *Thermal management*

The cell temperature rises significantly at the end of the discharging process due to the notable heat release from the occurring chemical reactions. As a result, the original cooling capacity is not sufficient to keep the temperature below the 340 °C limit in the case of the optimized state of charge profiles. Above that limit, side reactions may occur leading to thermal runaway situations, which must be prevented. In practice, this means that the nominal cooling power specified by the manufacturer poses constraints on the operation of the battery and does not allow to freely follow the optimized operation that would result in the highest economic benefits. Since cooling and heating constraints cannot be incorporated into linear optimization, cooling and heating power was adapted to the optimized operation. This is a major drawback of linear optimization, as one of the most important aspects of operation planning is to ensure proper thermal operation, but in this case, thermal operation was adapted to the optimization. Having said that, the possibilities of extending the cooling system of the battery in practice, as assumed in the simulation, should also be considered to increase flexibility of the operation.

This is performed by a sensitivity analysis, which found that the minimum cooling power that allows for respecting the temperature limits of 300–340 °C is 2300 W in Case 1 and 2400 W in Case 2. This means that double the original cooling capacity is necessary to allow for following the optimized profiles while respecting thermal constraints. Even though the safe operating range is between 300 and 350 °C, but the upper 10 °C is a transient zone, in which the charging and discharging

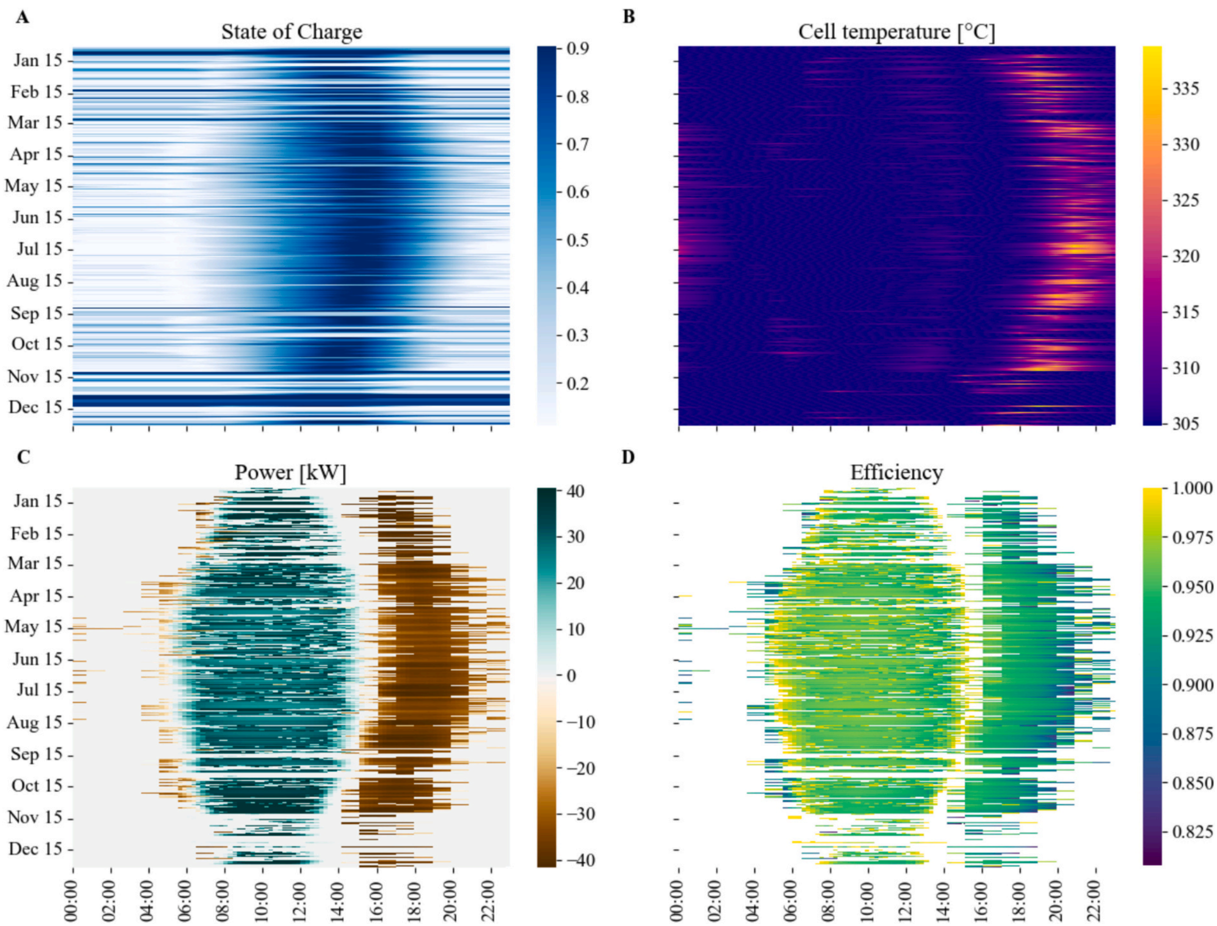

Fig. 7. Temporal evolution of the (A) state of charge, (B) cell temperature, (C) module charging/discharging power, and (D) battery efficiency for the total analyzed time period for the hybrid system (Case 1).

power of the battery is lowered to stay below the upper limit and ensure safe operation. That is the reason why the 300–340 °C is considered during the calculations and why the cooling power is sized in this way. All results related to the temperature of the battery and the thermal management are calculated with this 2400 W cooling power for both cases. Later, the operation in the transient range should also be considered and added to the model with different constraints.

The minimum temperature is 304.7 °C in both cases, the maximum values for Case 1 and Case 2 are 338.7 °C and 339.9 °C, while the average values are 306.9 °C and 307.5 °C, respectively. The annual energy demand of the cooling and heating are also calculated and shown in Table 2. The cooling and also the heating demand is higher in Case 1, which can be attributed to the different activity levels, as more frequent operation requires more cooling. Furthermore, the dependence on the PV system in case of Case 1 leads to lower activity levels at the beginning and at the end of the year, compared to Case 2 where this occurs only during the beginning of the year, leading to a slightly higher heating demand in Case 1. Overall, the electricity consumption of heating is more than ten times as much as that of cooling and the total energy demand of the thermal management system is slightly higher in Case 1.

The yearly heatmaps of the cell temperature are shown in Figs. 7B and 8B for the two cases, revealing that the temperature is close to the minimum during most of the time, and the temperature peaks appear at the end of the charging and discharging periods. The highest temperature peaks can always be observed at the end of discharging, since in discharging operation, the two sources of heat production in the battery, namely the dissipation on the internal resistances and the reaction term, are both positive and contribute to temperature rise. In contrast, the reaction term is negative during charging, which partially offsets the dissipation and results in only moderate heating or cooling demand.

Heatmaps are excellent for the compact visualization of whole yearly time series, however, it is hard to read the more nuanced differences from the color coding. To enhance visibility, Figs. 9 and 10 present the time series plots of the state of charge, module charging/discharging power, cell temperature, battery efficiency, and module heating and cooling power for the same 5-days period as shown in Figs. 5 and 6. The saw tooth profile in the cell temperature is the result of the switching operation of the module heating to keep the cell temperature above the lower limit during the stand-by and charging periods, when the thermal loss to the environment cannot be compensated with heat release from the operation. The charging resistance of the battery increases at high state of charge values, whereas the discharging resistance increases toward the lower state of charge values, both of which conditions correspond to the end of the respective battery operations [29]. This results in a sharp drop of efficiency in these conditions, which results in increased dissipation and a rapid increase in the cell temperature. For this reason, even though it is technically feasible to utilize the whole capacity, besides the lack of cell resistance reference data for the whole (0–100%) state of charge range, the battery operates between 10% and 90% in the model to ensure operation closer to the optimal.

4.3. Charging and discharging efficiency

The charging, discharging and round-trip efficiencies of the battery, calculated from the total yearly amounts of charged, stored, and discharged energy, are listed in Table 2. Both the charging and discharging efficiencies are slightly higher in Case 1, resulting in a round-trip efficiency of 87.84%, more than 1% higher than the 85.26% round-trip

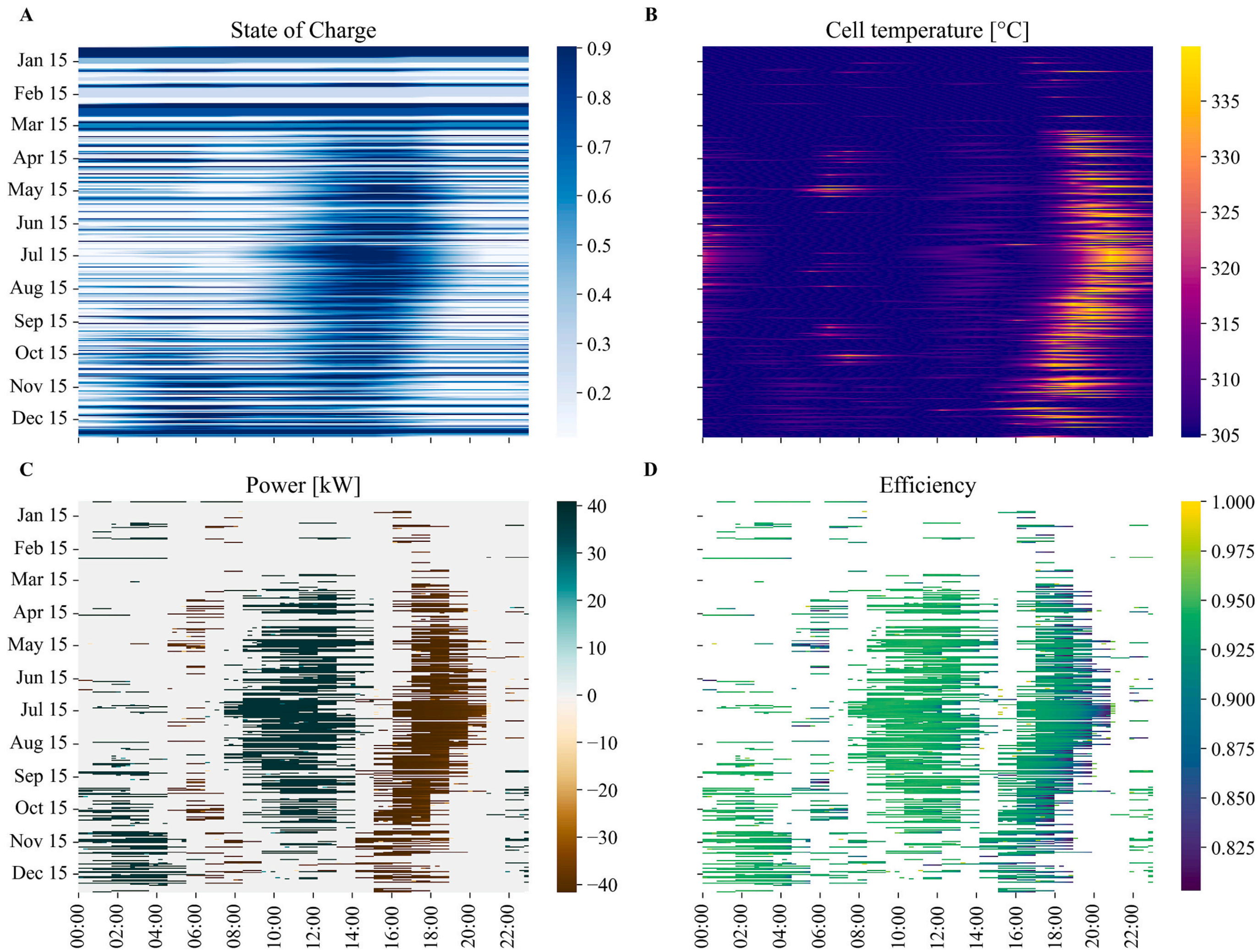

Fig. 8. Temporal evolution of the (A) state of charge, (B) cell temperature, (C) module charging/discharging power, and (D) battery efficiency for the total analyzed time period for the stand-alone battery (Case 2).

Table 2
Main characteristics of the battery operation in the two case studies.

Parameter	Case 1	Case 2
Charged energy	59.52 MWh	42.71 MWh
Discharged energy	52.29 MWh	36.41 MWh
Stored energy based on SOC	56.11 MWh	39.75 MWh
Number of equivalent cycles	200	141.5
Charging efficiency	94.25%	93.07%
Discharging efficiency	93.20%	91.60%
Round-trip efficiency	87.84%	85.26%
Maximum cell temperature	338.7 °C	339.9°C
Minimum cell temperature	304.7 °C	304.7 °C
Average cell temperature	306.9 °C	307.5 °C
Energy used for cooling	0.28 MWh	0.21 MWh
Energy used for heating	5.74 MWh	5.26 MWh
Share of energy used for cooling	0.49%	0.53%
Share of energy used for heating	10.23%	13,23%

efficiency in Case 2. This is partly attributed to the fact that the battery operates more frequently within the optimal range in terms of state of charge, where operation has lower losses. Furthermore, the operation in Case 1 can be considered somewhat more constant, as can be seen in Fig. 7.

In addition to the annual average values, the battery efficiencies are also calculated for every single time step when either charging or discharging happens based on the power and the change in state of charge, as described by Eqs. (17) and (18). These instantaneous efficiency values are shown of yearly heatmaps in Figs. 7D and 8D. Efficiency is relatively high during most of the charging period, but decreases toward its end. The discharging efficiency is slightly lower overall and drops to even lower values of around 80% at the end of discharging. The reasons for the reduced efficiencies are the increase of the internal resistances at high state of charge levels and higher temperatures. Overall, high temperatures have a negative impact on operation.

The sample efficiency time series plots in Figs. 9 and 10 show the previously mentioned reduction in charging and discharging efficiency by the end of the respective periods clearly for both cases. Finally, the presented analyses highlight that the currently applied logic of the thermal management system can produce contradictions, such as generating heating demand due to the overcooling of the module during short discharging periods. This can be observed on 14 May in both Figs. 9 and 10. Consequently, the logic of thermal management may require further revision in the future. It can also be seen that in the stand-alone case heating frequently switches on during stand-by mode to keep temperatures in the adequate range.

A limitation of the linear optimization method is that it calculates with constant efficiencies, which means that the effects of the state of charge, temperature, and charging power are not considered in the optimization and the resulting profiles. The dissipation losses on the

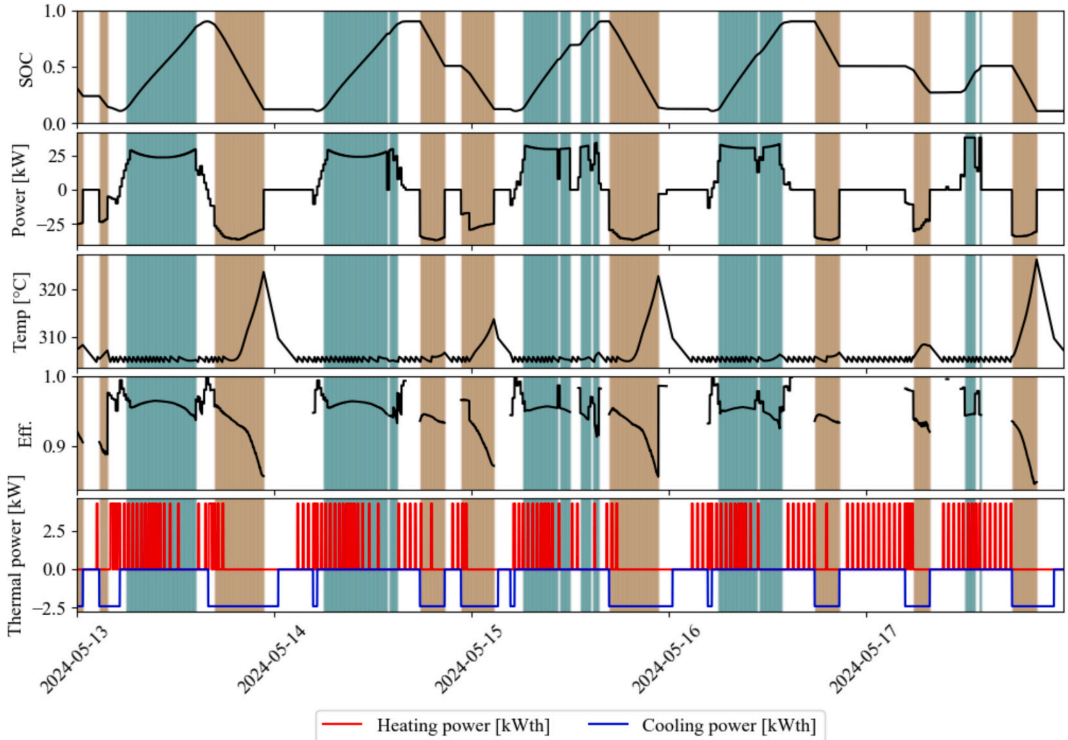

Fig. 9. Temporal evolution of the state of charge, module charging/discharging power, cell temperature, battery efficiency, and the module heating and cooling power for a selected week for the hybrid system (Case 1). Green, brown, and white backgrounds correspond to charging, discharging, and stand-by modes, respectively. (For interpretation of the references to color in this figure legend, the reader is referred to the web version of this article.)

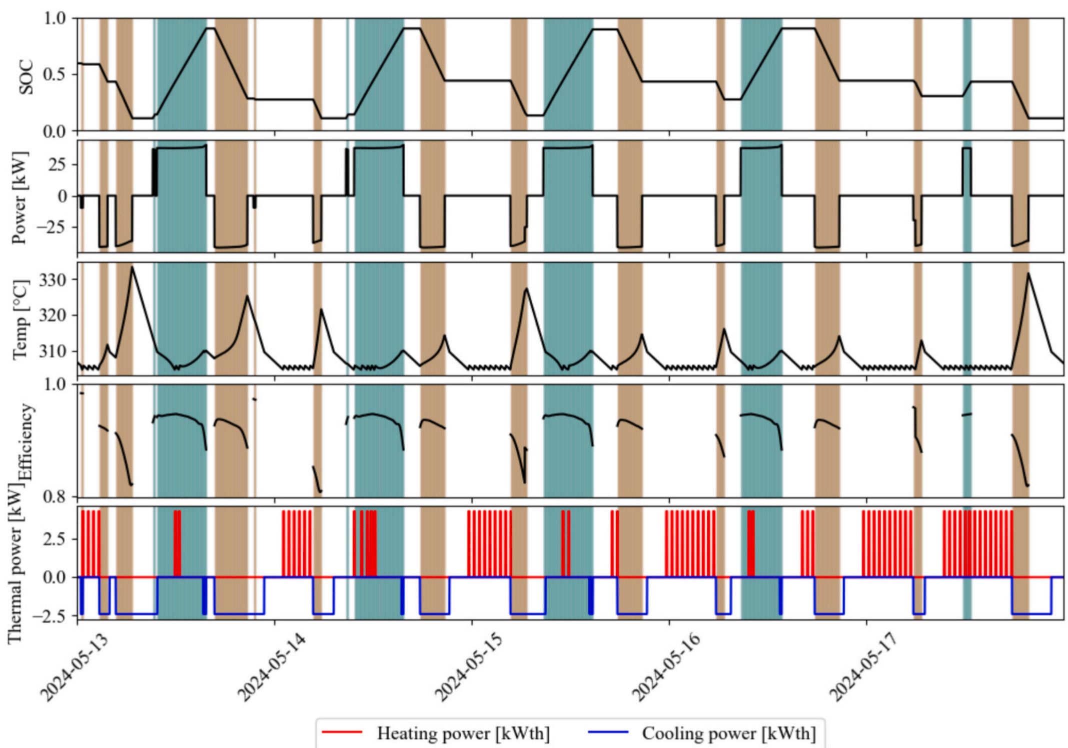

Fig. 10. Temporal evolution of the state of charge, module charging/discharging power, cell temperature, battery efficiency, and the module heating and cooling power for a selected week for the stand-alone battery (Case 2). Green, brown, and white backgrounds correspond to charging, discharging, and stand-by modes, respectively. (For interpretation of the references to color in this figure legend, the reader is referred to the web version of this article.)

internal resistances are proportional to the square of the charging or discharging current, therefore, operating the battery with lower power is a viable way of achieving higher round-trip efficiency. That said, due to the short-duration peaks in the market prices, prolonged charging and discharging periods would decrease the revenues even despite the efficiency improvements.

5. Conclusions

This study presents a comprehensive performance modeling framework for sodium-sulfur (NaS) batteries integrated with photovoltaic (PV) systems, emphasizing the importance of optimized charging and discharging strategies. A two-step methodology was developed, combining linear programming for system sizing and operational optimization with a reduced-order thermal-electrochemical battery model to evaluate the thermal behavior of the battery under realistic operating conditions. Two distinct case studies were analyzed: a hybrid PV-battery system designed to meet 50% of an annual 10 GWh electricity demand, and a stand-alone battery system optimized for electricity market arbitrage.

The results demonstrate that the proposed modeling approach effectively captures the complex interplay between energy flows, battery operation, and thermal dynamics. In the hybrid system (Case 1), the optimal configuration requires 5.43 MW of PV capacity and 10.11 MWh of battery storage, achieving a round-trip efficiency of 87.84% and maintaining cell temperatures within the safe operational range if the nominal cooling power is increased. However, significant PV curtailment was observed due to limited storage capacity. In contrast, the stand-alone battery (Case 2) exhibits less frequent cycling (141.5 cycles/year vs. 200 in Case 1), lower stored and discharged energy, and slightly lower round-trip efficiency (85.26%), driven by the goal of maximizing revenue through price arbitrage. Thermal analysis reveals that while both systems can remain within the acceptable temperature range if the nominal cooling power is increased, the amount of energy used for heating is notable compared to the energy stored during the investigated period. Note that these results are yearly specific values, meaning that for a greater freedom of operation, different cooling power might be necessary. A key insight from the study is the limitation of linear optimization in accounting for thermal constraints. The thermal management system had to be adapted post hoc to ensure safe operation, highlighting the need for integrated optimization frameworks that consider both electrochemical and thermal aspects simultaneously. Additionally, the analysis uncovered inefficiencies in the current thermal control logic, such as unnecessary heating following overcooling, suggesting room for improvement in control strategies.

Finally, we acknowledge that the optimization framework used in this study does not include thermal constraints explicitly. Future work should focus on enhancing the integration of thermal constraints directly into the optimization process, potentially through mixed-integer or nonlinear programming approaches, which are significantly more computationally intensive for year-long simulations. Given the goal of developing a tractable system-level planning tool, the present study therefore adopts a two-step approach in which thermal feasibility is evaluated after the economic optimization. While this structure is appropriate for long-horizon techno-economic analyses, future research may explore thermally integrated optimization methods to more tightly couple operational planning with the underlying physics of NaS battery behavior. Moreover, extending the model to include degradation mechanisms and real-time control strategies, potentially leveraging powerful AI models for forecasting and decision-making, would improve its applicability for long-term planning and operational decision-making. Furthermore, exploring the impact of evolving electricity market conditions, such as increasing occurrences of negative pricing, could further refine the economic viability of NaS battery systems in future energy landscapes.

CRediT authorship contribution statement

Botond Ilyés: Writing – original draft, Visualization, Software, Methodology, Investigation, Formal analysis, Data curation, Conceptualization. **Dávid Csemány:** Writing – original draft, Validation, Supervision, Software, Project administration, Methodology, Investigation, Formal analysis, Conceptualization. **Martin János Mayer:** Writing – original draft, Visualization, Supervision, Software, Resources, Methodology, Investigation, Funding acquisition, Formal analysis, Conceptualization.

Funding

This paper is supported by the National Research, Development and Innovation Fund, project no. OTKA-FK 142702, and in the frame of the 2021-2.1.1-EK-00002 project, by the Hungarian Academy of Sciences through the Sustainable Development and Technologies National Programme (FFT NP FTA), the János Bolyai Research Scholarship and the HUN-REN Centre for Energy Research Scholarship (EK2-HKUT).

Declaration of competing interest

The authors declare that they have no known competing financial interests or personal relationships that could have appeared to influence the work reported in this paper.

Appendix A

A time-resolution sensitivity analysis was conducted to assess whether the 1-min resampling of the optimized 15-min *SOC* profile provides sufficiently accurate thermal calculations, particularly considering the nonlinear heat generation and the switching behavior of the thermal controller. Six temporal resolutions (10 s, 30 s, 1 min, 2 min, 5 min, and the original 15 min) were evaluated for Case 1. For each resolution, key output quantities (identical to the ones presented in Table 2) were compared against the 1-min baseline. The relative difference (*RD*) was calculated with Eq. (A1):

$$RD = \frac{\xi_{ts} - \xi_{1min}}{\xi_{1min}} \cdot 100\% \quad \text{(A1)}$$

where ξ refers to the evaluated output quantity (e.g., charged energy), while subscripts *ts* and *1min* refer to the compared time step and 1-minute resolution, respectively. The results show that reducing the time step below 1 min yields no meaningful improvement in any of the evaluated metrics, while coarse resolutions (≥2 min) introduce noticeable deviations primarily in heating demand and peak temperature prediction. Furthermore, the temperature-time profiles associated with rapid transients were nearly indistinguishable between the 10 s, 30 s, and 1-min cases. This behavior is presented for a selected time period in Fig. A1. These findings confirm that the adopted 1-min resolution strikes an appropriate balance between numerical accuracy and computational feasibility.

Table A1
Relative difference values calculated by Eq. (A1) for Case 1 for different time steps. Please note that the values indicated by "ref" are presented in Table 2.

Parameter	10s	30s	1 min	2 min	5 min	15 min
Charged energy	0.30%	0.30%	ref.	0.05%	0.24%	0.08%
Discharged energy	0.27%	0.27%	ref.	0.71%	0.40%	0.63%
Stored energy based on SOC	0.18%	0.29%	ref.	0.11%	0.29%	0.29%
Number of equivalent cycles	0.15%	0.15%	ref.	0%	0.15%	0.15%
Charging efficiency	−0.01%	0%	ref.	0.08%	0.06%	0.21%
Discharging efficiency	−0.02%	−0.01%	ref.	0.57%	0.11%	0.34%
Round-trip efficiency	−0.02%	−0.02%	ref.	0.66%	0.15%	0.56%
Maximum cell temperature	0%	0%	ref.	−1.33%	0.10%	−0.06%
Minimum cell temperature	0.03%	0.03%	ref.	−0.03%	−0.16%	−0.59%
Average cell temperature	0%	0%	ref.	−0.03%	0.03%	0.07%
Energy used for cooling	3.57%	3.57%	ref.	7.14%	3.57%	3.57%
Energy used for heating	0%	0.17%	ref.	10.45%	1.74%	4.88%

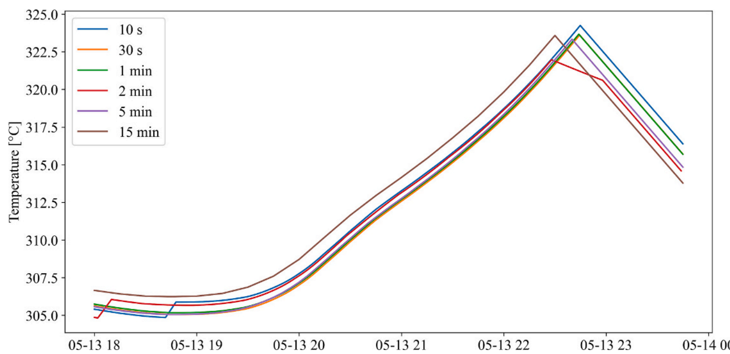

Fig. A1. Temperature-profiles corresponding to different time steps for a selected time period for Case 1.

Data availability

Data will be made available on request.

References

[1] J. Brodny, M. Tutak, Decade of progress: a multidimensional measurement and assessment of energy sustainability in EU-27 nations, Appl. Energy 382 (2025) 125222, https://doi.org/10.1016/j.apenergy.2024.125222.

[2] T.G. Teferi, T.G. Tella, S. Hampannavar, Impact of large-scale renewable energy integration on the grid voltage stability, Results Eng. 23 (2024) 102398, https://doi.org/10.1016/j.rineng.2024.102398.

[3] M. Jafarian, E. Assareh, A. Ershadi, X. Wang, Optimal integration of efficient energy storage and renewable sources in hybrid energy systems: a novel optimization and dynamic evaluation strategy, J. Energy Storage 101 (2024) 113880, https://doi.org/10.1016/j.est.2024.113880.

[4] B. Shi, Y. Yuan, S. Managi, Improved renewable energy storage, clean electrification and carbon mitigation in China: based on a CGE analysis, J. Clean. Prod. 418 (2023) 138222, https://doi.org/10.1016/j.jclepro.2023.138222.

[5] D. Kumar, S.K. Rajouria, S.B. Kuhar, D.K. Kanchan, Progress and prospects of sodium-sulfur batteries: a review, Solid State Ionics 312 (2017) 8–16, https://doi.org/10.1016/j.ssi.2017.10.004.

[6] M. Vins, M. Sirovy, Sodium-sulfur batteries for energy storage applications, in: 2019 20th Int. Sci. Conf. Electr. Power Eng, 2019, pp. 1–5, https://doi.org/10.1109/EPE.2019.8778134.

[7] M. Alqarni, Sodium sulfur batteries allocation in high renewable penetration microgrids using coronavirus herd immunity optimization, Ain Shams Eng. J. 13 (2022) 101590, https://doi.org/10.1016/j.asej.2021.09.017.

[8] Y. Liang, B. Zhang, Y. Shi, R. Jiang, H. Zhang, Research on wide-temperature rechargeable sodium-sulfur batteries: features, challenges and solutions, Materials (Basel). 16 (2023), https://doi.org/10.3390/ma16124263.

[9] A. Bhattacharjee, H. Saha, Development of an efficient thermal management system for Vanadium Redox Flow Battery under different charge-discharge conditions, Appl. Energy 230 (2018) 1182–1192, https://doi.org/10.1016/j.apenergy.2018.09.056.

[10] B. Xu, J. Li, Y. Xie, Q. Gui, Q. Wu, W. Liu, L. Mao, Capacity degradation study of NaNi1/3Fe1/3Mn1/3O2 cathode sodium-ion batteries induced by overcharge, J. Power Sources 623 (2024) 235448, https://doi.org/10.1016/j.jpowsour.2024.235448.

[11] H. Zhou, A.S. Alujjage, M. Terese, C. Fear, T. Joshi, V.R. Rikka, J.A. Jeevarajan, P. P. Mukherjee, Effect of fast charging on degradation and safety characteristics of lithium-ion batteries with LiFePO4 cathodes, Appl. Energy 377 (2025) 124465, https://doi.org/10.1016/j.apenergy.2024.124465.

[12] Y. Wang, F. Liao, J. Bi, C. Lu, Optimal battery electric bus system planning considering heterogeneous vehicles, opportunity charging, and battery degradation, Renew. Energy 237 (2024) 121596, https://doi.org/10.1016/j.renene.2024.121596.

[13] S. Hong, D. Ma, W. Zeng, J. Shi, Y. Liu, L. Yang, Y. Fan, Y. Liu, C. Yang, B. Hong, Optimization of fast-charging strategy for LISHEN 4695 cylindrical lithium-ion batteries, J. Power Sources 629 (2025) 236013, https://doi.org/10.1016/j.jpowsour.2024.236013.

[14] C. Cienfuegos, P.M. Rodrigo, I. Cienfuegos, A. Diaz-Ponce, Comparative analysis of battery energy storage systems' operation strategies for peak shaving in industries with or without installed photovoltaic capacity, Renew. Energy Focus. 49 (2024) 100574, https://doi.org/10.1016/j.ref.2024.100574.

[15] G. Madhusudanan, S. Padhmanabhaiyappan, Solar power fluctuation smoothing through battery energy storage system using AVOA-SAGAN approach, J. Energy Storage 101 (2024) 113610, https://doi.org/10.1016/j.est.2024.113610.

[16] P.M. Attia, A. Grover, N. Jin, K.A. Severson, T.M. Markov, Y.-H. Liao, M.H. Chen, B. Cheong, N. Perkins, Z. Yang, P.K. Herring, M. Aykol, S.J. Harris, R.D. Braatz, S. Ermon, W.C. Chueh, Closed-loop optimization of fast-charging protocols for batteries with machine learning, Nature 578 (2020) 397–402, https://doi.org/10.1038/s41586-020-1994-5.

[17] M. Yang, S. Chen, Y. Jia, L. Ouyang, The review of sodium and potassium-ion battery advances in density functional theory: progresses, challenges and prospects, Mater. Sci. Eng. R. Rep. 167 (2026) 101097, https://doi.org/10.1016/j.mser.2025.101097.

[18] R. Zhang, M. Lee, L. Huang, M. Ni, Optimization of battery energy storage system (BESS) sizing in different electricity market types considering BESS utilization mechanisms and ownerships, J. Clean. Prod. 470 (2024) 143317, https://doi.org/10.1016/j.jclepro.2024.143317.

[19] T. Dias de Lima, P. Faria, Z. Vale, Optimizing home energy management systems: a mixed integer linear programming model considering battery cycle degradation, Energ. Buildings 329 (2025) 115251, https://doi.org/10.1016/j.enbuild.2024.115251.

[20] C. Fan, M. Lu, Y. Sun, D. Liang, A novel linear programming-based predictive control method for building battery operations with reduced cost and enhanced computational efficiency, Renew. Energy 237 (2024) 121847, https://doi.org/10.1016/j.renene.2024.121847.

[21] D. Cremoncini, G.F. Frate, A. Bischi, L. Ferrari, Mixed Integer Linear Program model for optimized scheduling of a vanadium redox flow battery with variable efficiencies, capacity fade, and electrolyte maintenance, J. Energy Storage 59 (2023) 106500, https://doi.org/10.1016/j.est.2022.106500.

[22] M. Amini, M.H. Nazari, S.H. Hosseinian, Optimal energy management of battery with high wind energy penetration: a comprehensive linear battery degradation

cost model, Sustain. Cities Soc. 93 (2023) 104492, https://doi.org/10.1016/j.scs.2023.104492.
[23] N.Q. Minh, N.D. Linh, N.T. Khiem, A mixed-integer linear programming model for microgrid optimal scheduling considering BESS degradation and RES uncertainty, J. Energy Storage 104 (2024) 114663, https://doi.org/10.1016/j.est.2024.114663.
[24] G. Nikiforidis, M.C.M. van de Sanden, M.N. Tsampas, High and intermediate temperature sodium–sulfur batteries for energy storage: development, challenges and perspectives, RSC Adv. 9 (2019) 5649–5673, https://doi.org/10.1039/C8RA08658C.
[25] J.K. Min, M. Stackpool, C.H. Shin, C.-H. Lee, Cell safety analysis of a molten sodium–sulfur battery under failure mode from a fracture in the solid electrolyte, J. Power Sources 293 (2015) 835–845, https://doi.org/10.1016/j.jpowsour.2015.05.119.
[26] S. Schaefer, S.P. Vudata, D. Bhattacharyya, R. Turton, Transient modeling and simulation of a nonisothermal sodium–sulfur cell, J. Power Sources 453 (2020) 227849, https://doi.org/10.1016/j.jpowsour.2020.227849.
[27] S.P. Vudata, D. Bhattacharyya, Thermal management of a high temperature sodium sulphur battery stack, Int. J. Heat Mass Transf. 181 (2021) 122025, https://doi.org/10.1016/j.ijheatmasstransfer.2021.122025.
[28] J.K. Min, C.-H. Lee, Numerical study on the thermal management system of a molten sodium-sulfur battery module, J. Power Sources 210 (2012) 101–109, https://doi.org/10.1016/j.jpowsour.2012.03.028.
[29] D. Csemány, Coupled thermal-electrical lumped parameter modeling of high-temperature sodium-sulfur battery, J. Energy Storage 109 (2025) 115117, https://doi.org/10.1016/j.est.2024.115117.
[30] L. Deguenon, D. Yamegueu, S. Moussa kadri, A. Gomna, Overcoming the challenges of integrating variable renewable energy to the grid: a comprehensive review of electrochemical battery storage systems, J. Power Sources 580 (2023) 233343, https://doi.org/10.1016/j.jpowsour.2023.233343.
[31] Z. Zhang, T. Ding, Q. Zhou, Y. Sun, M. Qu, Z. Zeng, Y. Ju, L. Li, K. Wang, F. Chi, A review of technologies and applications on versatile energy storage systems, Renew. Sust. Energ. Rev. 148 (2021) 111263, https://doi.org/10.1016/j.rser.2021.111263.
[32] A.A. Kebede, T. Kalogiannis, J. Van Mierlo, M. Berecibar, A comprehensive review of stationary energy storage devices for large scale renewable energy sources grid integration, Renew. Sust. Energ. Rev. 159 (2022) 112213, https://doi.org/10.1016/j.rser.2022.112213.
[33] Z.F. Hussien, L.W. Cheung, M.F.M. Siam, A.B. Ismail, Modeling of sodium sulfur battery for power system applications, Elektrika 9 (2007) 66–77.
[34] D. Yang, X. Xia, M.J. Mayer, A tutorial review of the solar power curve: regressions, model chains, and their hybridization and probabilistic extensions, Adv. Atmos. Sci. 41 (2024) 1023–1067, https://doi.org/10.1007/s00376-024-3229-4.
[35] Z. Šimić, D. Topić, G. Knežević, D. Pelin, Battery energy storage technologies overview, Int. J. Electr. Comput. Eng. Syst. 12 (2021) 53–65, https://doi.org/10.32985/ijeces.12.1.6.
[36] G. Yang, D. Yang, C. Lyu, W. Wang, N. Huang, J. Kleissl, M.J. Perez, R. Perez, D. Srinivasan, Implications of future price trends and interannual resource uncertainty on firm solar power delivery with photovoltaic overbuilding and battery storage, IEEE Trans. Sustain. Energy. 14 (2023) 2036–2048, https://doi.org/10.1109/TSTE.2023.3274109.
[37] M. Perez, R. Perez, K.R. Rábago, M. Putnam, Overbuilding & curtailment: the cost-effective enablers of firm PV generation, Sol. Energy 180 (2019) 412–422, https://doi.org/10.1016/j.solener.2018.12.074.